Origin of the thermal expansion anomaly in layered Bi_2X_3 topological insulators: Ultrafast time-resolved pump-probe experiments and theory

Gyan Prakash,[1] Koushik Pal,[2] Manish Jain,[3] U. V. Waghmare,[2] and A. K. Sood[1,*]

[1]*Department of Physics and Center for Ultrafast Laser Applications, Indian Institute of Science, Bangalore 560012, India*

[2]*Theoretical Sciences Unit, Jawaharlal Nehru Centre for Advanced Scientific Research, Jakkur Campus, Bangalore 560064, India*

[3]*Department of Physics, Indian Institute of Science, Bangalore 560012, India*

(Received 29 April 2017; published 7 August 2017)

Recent experiments on the thermal expansion of Sb_2Te_3, a prototypical example of strong three-dimensional topological insulators, have shown an intriguing anomaly in the thermal expansion coefficient along the hexagonal axis ($\alpha_\parallel$), which drops sharply to almost zero in a narrow range of temperature around ∼225 K. With no accompanying signatures in other properties, the origin of this anomaly is not understood. We present here femtosecond pump-probe differential reflectivity measurements on single crystals of Sb_2Te_3 as a function of temperature from 3 to 300 K to determine the temperature dependence of coherent optical and acoustic phonons along with the dynamics of the photoexcited carriers. We find clearly anomalous temperature dependence of the parameters associated with vibrational and electronic relaxation in the narrow temperature range of 200–250 K. Within first-principles density functional theoretical analysis, we show that the observed anomalies can be explained with a mechanism of formation of stacking faults stabilized by vibrational entropy above 200 K. As a similar anomaly in the thermal expansion is also observed in other chalcogenides in the same family, the proposed mechanism may also be applicable to these layered strong topological insulators.

DOI: 10.1103/PhysRevB.96.075109

I. INTRODUCTION

Starting from $Bi_{1-x}Sb_x$ as a three-dimensional topological insulator (3D-TI) [1–3], Sb_2Te_3, Bi_2Te_3, and Bi_2Se_3 were identified as 3D-TIs in the same crystal family with a single surface Dirac cone [4–7]. These compounds have layered structures with quintuple layers of the formula unit stacked along c axis which are held together by weak van der Waals interaction. In recent years, most experimental measurements on TI focused on surface electronic structure and investigations of their bulk properties have remained relatively scarce. Recent x-ray diffraction and dilatometry experiments have shown an intriguing anomaly in the thermal expansion coefficients of bulk Sb_2Te_3 [8] and Bi_2Se_3[9], without any structural or electronic phase transition. The coefficient of linear thermal expansion along the trigonal c axis ($\alpha_\parallel$) in Sb_2Te_3 deviates significantly from the Debye law in the temperature region of 200–240 K. It decreases sharply within the range showing a minimum at 225 K (even crosses zero and becomes negative) and then increases abruptly in the temperature region 225–236 K. Importantly, the specific heat measurements do not show any corresponding anomaly in this temperature range. A similar anomalous behavior of thermal expansion has also been seen for Bi_2Te_3 [10].

As no other physical property has been shown so far to display anomalous temperature dependence in this range, the origin of the observed anomaly in the thermal expansion coefficient is unclear. The aim of the present work is to experimentally probe coherent optical and acoustic phonons along with the relaxation dynamics of the photoexcited carriers in Sb_2Te_3 over the complete range of 3 to 300 K using ultrafast time-resolved pump-probe experiments. In particular, we are interested in finding signatures, if any, of anomalous temperature dependence of phonon and electron dynamics and provide a theoretical framework to explain the anomaly.

We use ultrafast pump pulses of energy (1.57 eV) above the band gap of Sb_2Te_3 to generate nonequilibrium electron-hole excitations. The transient differential reflectivity $\Delta R(t)/R_0$ is monitored by a weaker time-delayed probe pulse as a function of time delay. Together with electronic excitation, coherent optical phonons are generated due to displacive excitation of coherent phonons (DECP) in opaque materials [11]. Our experiments show that the frequency of A^1_{1g} optical phonon decreases near the anomaly temperature ($T_a \sim 225$ K). A significant deviation in the temperature dependence of the frequency shift from the cubic anharmonic decay and thermal expansion contribution is observed.

The pump laser also induces transient electronic and thermal stresses at the surface of the sample which is responsible for the generation of coherent acoustic phonons [12,13]. A strain pulse launched by the pump pulse at the surface propagates into the bulk with longitudinal sound velocity (v_{LA}). It is expected that structural changes with temperature in anomalous thermal expansion range will affect the optical properties, sound velocity, and modulus of elasticity. Using the strain pulse propagation model we extract the refractive index (n), longitudinal modulus of elasticity (Y_{LA}), and longitudinal sound velocity (v_{LA}) as a function of temperature [13,14]. A large change of about ∼97% in v_{LA} is observed around T_a. With first-principles density functional theory (DFT) calculations, we examine various possibilities to understand the observed anomaly. We propose a mechanism associated with the formation of stacking faults (SFs) in the layered structure of Sb_2Te_3, which becomes energetically favorable above the temperature of the observed anomaly. Our theoretical results qualitatively explain the observed variation in n, v_{LA}, and corresponding Y_{LA} near T_a identifying the structural origin of the anomaly.

*Corresponding author: asood@physics.iisc.ernet.in

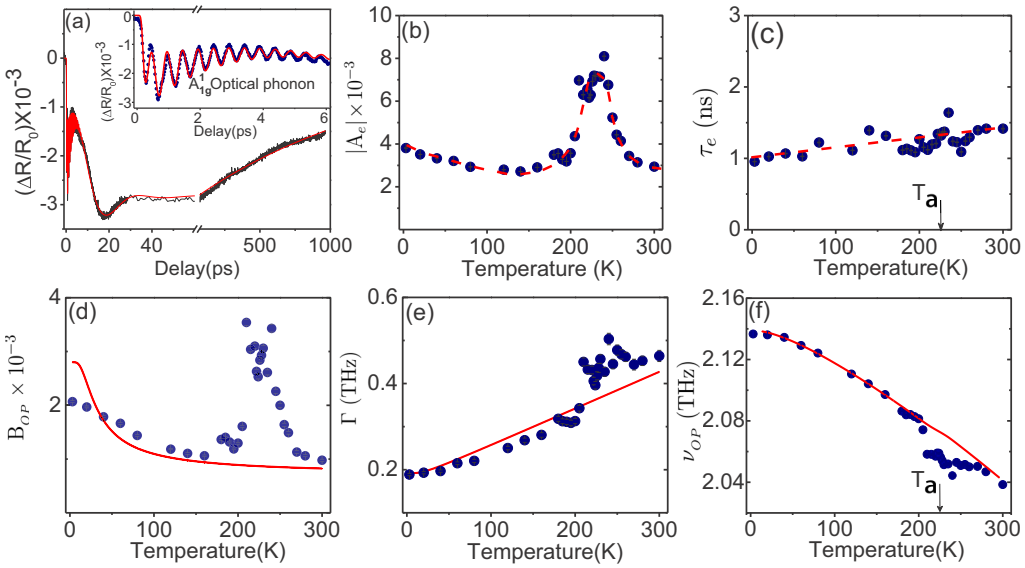

FIG. 1. (a) $\Delta R/R_0$ signal at 300 K showing different processes: excited carrier relaxation, coherent optical phonon A^1_{1g}, and acoustic phonon. Solid line is the fit as discussed in text. Inset shows zoomed view of A^1_{1g} optical phonon oscillations with solid lines (red color) as fit. Temperature dependence of (b) initial amplitude A_e and (c) carrier relaxation time τ_e (dashed lines in red color joining through data points are guide to eye). Optical phonon A^1_{1g} (d) oscillation amplitude B_{OP} (e) scattering rate Γ and (f) frequency ν_{OP} as a function of temperature. Solid lines (red color) in (d) and (e) are fit with cubic anharmonicity model for B_{OP} and Γ. Solid line (red) in (f) is fit to frequency shift with temperature by cubic anharmonic model together with thermal expansion contribution. Error bars are smaller than symbol size.

II. EXPERIMENTAL DETAILS

A single crystal of Sb_2Te_3 ($6\times5\times0.5\,mm^3$) with a fresh cleaved surface normal to trigonal c axis was mounted on the cold finger of a continuous helium flow optical cryostat (Oxford Instruments, Microstat He). Degenerate optical pump probe experiments were done with pulses of central photon energy 1.57 eV derived from Ti:sapphire amplifier (Spitfire, Spectra Physics Inc.) at 1 KHz repetition rate. The spot size of the pump and probe lasers were ∼1.03 and 0.86 mm [full width at half maximum (FWHM)], respectively. The laser pulse width was measured to be ∼78 fs (FWHM) at the sample point. The pump and probe polarizations were kept orthogonal and an analyzer orthogonal to pump polarization was kept at the detector to prevent scattered pump light from reaching the detector. Both pump and probe beams were incident close to normal on the crystal. During the entire temperature-dependent experiments, the pump and probe polarization, angle of incidence, and orientation of crystal inside the cryostat were kept fixed. A lock-in amplifier slaved to the modulation frequency of the pump laser (at 257 Hz) was used to improve the signal to noise ratio. The transient differential reflectivity signals were recorded for several temperatures between 3 to 300 K at a pump fluence of $702\,\mu J/cm^2$.

III. RESULTS AND DISCUSSION

The Sb_2Te_3 crystal, a layered structure with space group $R\bar{3}m$ (No. 166), is made up of closed-packed atomic layers which are periodically stacked along the c axis with a unit of five atomic planes ($Te^{(1)}$-Sb-$Te^{(2)}$-Sb-$Te^{(3)}$) called a quintuple. These layers are bonded by weak van der Waals force [15,16]. There are five atoms in the rhombohedral unit cell of Sb_2Te_3 [15,16]. Group theoretical analysis of the symmetry of the centrosymmetric rhombohedral (D^5_{3d}) Sb_2Te_3 crystal predicts 12 optical phonons at the Γ point with irreducible representations as $2A_{1g}(R)+2E_g(R)+2A_{2u}(IR)+2E_u(IR)$ [16], where R and IR refer to the Raman and infrared active modes, respectively [15–17]. The frequencies of the A_{1g} modes at 80 K are $72\,cm^{-1}$ (2.16 THz) and $174.5\,cm^{-1}$ (5.23 THz) and those of the E_g modes are $43\,cm^{-1}$ (1.29 THz) and $131.5\,cm^{-1}$ (3.94 THz) [15,17].

Figure 1(a) shows $\Delta R(t)/R_0$ at 300 K. The $\Delta R(t)/R_0$ signal shows a fast and a slow oscillatory component superimposed on a background of an exponentially decaying component which arises from the relaxation of photoexcited charge carriers. The fast oscillatory component has a frequency of 2.04 THz ($68\,cm^{-1}$) and is attributed to the A^1_{1g} optical phonon, in agreement with the reported ultrafast and Raman results on Sb_2Te_3 [15–19]. The slow oscillation of frequency ∼34 GHz is attributed to coherent longitudinal acoustic phonons. To determine the temperature dependence of the electronic relaxation parameters, optical and acoustic phonon frequencies, amplitude and damping time, the transient differential reflectivity $\Delta R/R_0$ signals at each temperature are fitted with the following function convoluted with a Gaussian laser pulse

$$\frac{\Delta R}{R_0} = (1-e^{-t/t_r})\{A_e e^{-t/\tau_e} + B_{OP}e^{-t/\tau_{OP}}\cos(2\pi\nu_{OP}t+\phi_{OP}) + B_{LA}e^{-t/\tau_{LA}}\cos(2\pi\nu_{LA}t+\phi_{LA})\}. \quad (1)$$

The term $(1-e^{-t/t_r})$ represents the initial rise of the $\Delta R/R_0$ signal. The rise time t_r is the time taken to attain the maximum value of $\Delta R/R_0$ after the pump excitation. The $\Delta R/R_0$ signal takes ∼77 fs to reach its maximum value, corresponding to the rapid thermalization of excited carriers.

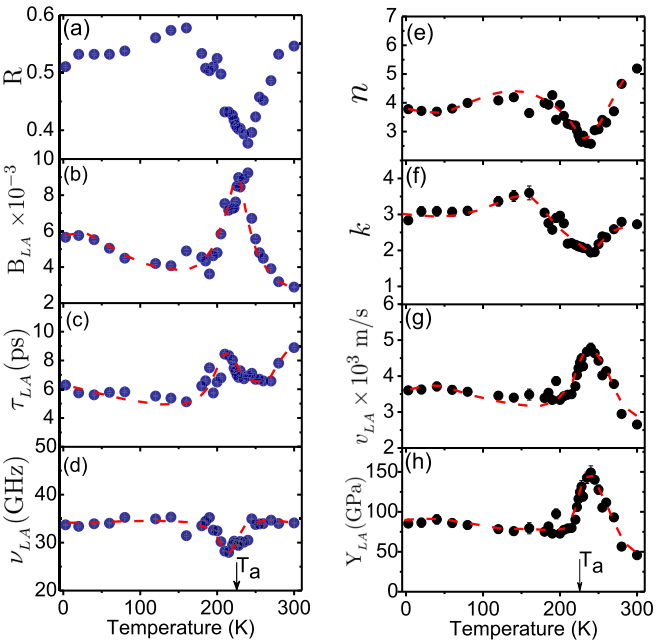

FIG. 2. Temperature dependence of (a) reflectivity R, longitudinal acoustic phonon (b) initial amplitude B_{LA}, (c) dephasing time τ_{LA}, and (d) frequency of oscillations ν_{LA} obtained by fitting differential reflectivity signals $\Delta R/R_0$ at each temperature. Obtained temperature dependence of optical constants (e) refractive index n, (f) extinction coefficient k, (g) sound velocity v_{LA}, and (h) longitudinal modulus of elasticity Y_{LA}. Dashed lines joining through data points are guide to eye. Error bars are smaller than symbol size.

A_e and τ_e^{-1} are the amplitude and decay rate of photoexcited charge carriers. We see a single exponential relaxation kinetics with decay rate (τ_e^{-1}) of ns duration [Fig. 1(c)]. The expected electron-optical phonon mediated relaxation (∼1.5−3.1 ps)(as seen in Bi_2Se_3 thin films without optical phonons [20]) is not well resolved due to the presence of the oscillatory component due to coherent optical phonons. The rate of relaxation (τ_e^{-1}) cannot be attributed to the heat leaving the probe spot. This can be confirmed by calculating the lattice heat diffusion time given by $t_D = l_d^2/K$, where l_d is the diffusion length and K is therml diffusivity. Thermal diffusivity is given by [21] $K = \kappa/\rho C$ where $\kappa = 40.72\,\mathrm{mw\,cm^{-1}\,{}^\circ C^{-1}}$ is thermal conductivity [22], $\rho = 6.51\,\mathrm{g/cm^3}$ is density, and $C = 125\,\mathrm{J\,mole^{-1}\,K^{-1}}$ is specific heat [8]. Taking diffusion length as the penetration depth of probe beam [23] ∼11 nm gives the characteristic diffusion time of ∼39 ps. We attribute the relaxation time (τ_e^{-1}) to the localization of photoexcited carriers and their recombination, in agreement with the slow relaxation on the ns scale observed in Bi_2Se_3 [20]. The amplitude $|A_e|$ (related to the change in probe reflectivity modulated by the thermalized carriers) attains a maximum value at $T_a \sim 225$ K and decreases steadily for T ⩾ 225 K, showing a significant change, greater than three-fold, in the amplitude [Fig. 1(b)]. This change in $|A_e|$ is related to the decrease in reflectivity of the pump beam as will be discussed later [Fig. 2(a)]. Although a gradual increase in τ_e (from 1 ns at 3 K to 1.5 ns at 300 K) can be observed in Fig. 1(c), analysis of the temperature dependence of the electronic relaxation is not the focus of this work. The parameters B_{OP} (B_{LA}), τ_{OP} (τ_{LA}), ν_{OP} (ν_{LA}), and ϕ_{OP} (ϕ_{LA}) are amplitude, damping time, frequency, and phase of the coherent optical (acoustic) phonons, respectively. The fit was found to be excellent over the entire temperature range.

Figures 1(d), 1(e), and 1(f) show the temperature dependence of B_{OP}, Γ (τ_{OP}^{-1}), and ν_{OP}, respectively. The temperature dependence of the optical phonon frequency and scattering rate is given by the well-known cubic anharmonic decay model [24–26]. The amplitude of the coherent optical phonons observed in ultrafast experiments varies similarly to the Raman peak intensity [27]. Since the Raman cross section for a phonon of frequency $\nu_0 \propto [n(\nu_0)+1]$, where $n(\nu_0) = [\exp(\frac{h\nu_0}{k_BT}) - 1]^{-1}$ is the Bose-Einstein factor and the scattering rate $\Gamma(T) \sim [2n(\nu_0/2)+1]$, the coherent phonon amplitude should vary as $\sim\frac{n(\nu_0)+1}{2n(\nu_0/2)+1}$, as shown by the solid line in Fig. 1(d).

We clearly see that the amplitude B_{OP} is anomalous near $T_a \sim 225$ K (∼335% higher than the cubic anharmonic fit). Figure 1(e) shows scattering rate Γ (τ_{OP}^{-1}) of the A_{1g}^1 coherent optical phonon as a function of lattice temperature T. The value of the scattering rate at room temperature is 0.45 THz which agrees well with the results in Ref. [28]. We note that the scattering rates as measured by Raman scattering are higher in Sb_2Te_3 [29] as compared to Bi_2Se_3 [29,40] and Bi_2Te_3 [40]. According to the cubic anharmonicity model, the scattering rate of the optical phonon of frequency ν_0 is given as $\Gamma(T) = \Gamma_0 + C[2n(\nu_0/2)+1]$ [24] where Γ_0 is the disorder-induced temperature-independent decay rate and C is related to phonon-phonon interaction. The solid line in Fig. 1(e) is a fit with $\Gamma_0 = 0.17 \pm 0.01$ THz, $C = 0.022 \pm 0.001$ THz, and $\nu_0 = 2.142 \pm 0.001$ THz. The anharmonic model agrees well below 200 K, but fails to capture the anomalous increase close to T_a. Figure 1(f) shows the temperature dependence of the optical phonon frequency ν_{OP}. The frequency shift with temperature can be well described by cubic anharmonicity, but a more accurate description should include the quasiharmonic contribution to the shift due to thermal expansion, i.e., $\nu_{OP}(T) = \nu_0 + \Delta\nu^{(1)}(T) + \Delta\nu^{(2)}(T)$. $\Delta\nu^{(1)} = A[2n(\nu_0/2)+1]$ is the cubic anharmonic contribution with A as the measure of the strength of the cubic anharmonicity and $\Delta\nu^{(2)}$ is the contribution to the frequency shift solely due to the volume expansion [29–32] given by

$$\Delta\nu^{(2)}(T) = \nu_0\left[\exp\left(-\gamma\int_0^T\left[\alpha_\parallel(T') + 2\alpha_\perp(T')\right]dT'\right) - 1\right], \tag{2}$$

where $\gamma = 2.3$ is the mode Grüeinsen parameter [9] of the mode, $\alpha_\perp(T)$ and $\alpha_\parallel(T)$ are the coefficients of thermal expansion along the a and c axes of the hexagonal lattice, respectively. $\alpha_\parallel(T)$ has been taken from the thermal expansion results [8]. We take the lattice parameter $a(T)$ from Refs. [9,29] to calculate $\alpha_\perp(T)$. The solid line in Fig. 1(f) is a fit to the parameters $A = -0.0041 \pm 0.0001$ THz and $\nu_0 = 2.142 \pm 0.001$ THz. We see that the contribution of anomalous thermal expansion at T_a is only 0.003 THz and hence its contribution to the frequency shift does not capture the data between 200 to 250 K.

We now investigate the slow oscillation observed in $\Delta R/R_0$ traces (Fig. 2) attributed to stress-generated longitudinal acoustic pulse propagating into the bulk with sound velocity

(v_{LA}) [13]. Following the Thomsen model [13], the probe reflectivity change owing to the strain pulse is given by

$$\Delta R \propto \cos\left(\frac{4\pi n v_{LA} t}{\lambda} - \delta\right) e^{-z/\xi}, \quad (3)$$

with δ being the phase shift, n and k are the real and imaginary parts of the refractive index, $n^* = n + ik$, $\xi = \lambda/4\pi k$ is the probe penetration length, v_{LA} the sound velocity, and λ is the probe wavelength. Figures 2(b), 2(c) and 2(d) show the temperature dependence of B_{LA}, τ_{LA}, and v_{LA}, respectively. We see more than two-fold higher acoustic phonon amplitude B_{LA} at $T_a \sim 225$ K, showing the strongest pump-induced strain pulse launched at the anomaly temperature. The reflectivity of the sample at $\lambda = 790$ nm (1.57 eV), keeping the pump pulse blocked, was measured at each temperature, [Fig. 2(a)]. Noteworthy is a large drop in reflection near 225 K. Using $R(T)$, $v_{LA}(T)$, and $\tau_{LA}(T)$ in the strain propagation model (see Ref. [14]) we obtain the refractive index $n(T)$, $k(T)$, and $v_{LA}(T)$ as shown in Figs. 2(e) and 2(g). v_{LA} at room temperature is 2.7×10^3 m/s, in good agreement with the reported value [33]. The longitudinal modulus of elasticity related to the LA mode along the c axis is given by $Y_{LA}(T) = v_{LA}^2(T)\rho(T)$, where $\rho(T)$ is density calculated using the temperature dependence of the lattice parameters of Sb_2Te_3 [8,29]. Figure 2(h) shows that Y_{LA} at room temperature is 47.2 GPa, in close agreement with the reported value of 44.8 GPa [34]. Near T_a, a significant decrease is observed in n and k, while the v_{LA} and Y_{LA} show a significant increase near T_a.

To uncover the origin of anomalous temperature dependence of the experimentally observed quantities, e.g., $n(T)$, $Y_{LA}(T)$, we analyzed the structural, electronic, and vibrational properties of Sb_2Te_3 as a function of temperature using DFT calculations. As the Kohn-Sham DFT is a ground-state theory and it cannot directly (without molecular dynamics) take into account the effect of temperature, we incorporated temperature dependence in our calculations using experimental temperature-dependent lattice constants [$a(T)$ and $c(T)$]. We used the QUANTUM ESPRESSO (QE) [35] code which treats only the valence electrons, replacing the potential of ionic cores with smooth pseudopotentials. We used fully relativistic (to take into account the effect of spin orbit coupling) and scalar relativistic norm-conserving pseudopotentials treating the exchange-correlation energy functional with a generalized gradient approximation (GGA) [36]. Since strong spin-orbit coupling (SOC) is responsible for nontrivial electronic topology [37,38], we included SOC while calculating the electronic structure of Sb_2Te_3. Our calculation of phonons at a fixed lattice constant both with and without SOC reveals that the change in the phonon frequencies is quite small (~ 1 cm^{-1}). As calculations of phonons with SOC are computationally quite expensive, we calculated the phonon frequencies of Sb_2Te_3 without including SOC. We truncated the plane wave basis used in the expansion of the Kohn-Sham wave functions and the charge density with energy cutoffs of 60 and 240 Ry, respectively. We used $9 \times 9 \times 9$ and $12 \times 12 \times 2$ uniform grids of k points for sampling the Brillouin zone integrations of the rhombohedral and hexagonal unit cells, respectively, in self-consistent field (SCF) calculations along with the occupation number of electrons smeared with the Fermi-Dirac distribution function. We used the DFT linear response with PH package, available within QE, to determine the phonon frequencies [35]. The high frequency dielectric constant (ϵ_∞) (and hence refractive index $n = \sqrt{\epsilon_\infty}$) is calculated first without SOC using the linear response theory, keeping the occupation numbers of the electrons fixed, and was scissor-corrected to take into account the effect of SOC through the band gap using $n_{\rm SOC} = n_{\rm NSOC}\frac{E_g^{\rm SOC}}{E_g^{\rm NSOC}}$, where n is the refractive index, E_g is the band gap, SOC and NSOC indicate whether a quantity is calculated with (SOC) and without (NSOC) spin-orbit interaction, respectively. The longitudinal modulus of elasticity is calculated as the second derivative of the total energy (calculated with SOC) with respect to the uniaxial strain (ϵ_{zz}) in the hexagonal structures. We used the nudged elastic band (NEB)-climbing image (CI) procedure (without taking into account the effect of SOC) to search for the occurrences of isostructural phase transition in Sb_2Te_3.

Taking the temperature-dependent experimental lattice constants of Sb_2Te_3 [8,29], we fully relaxed the atomic positions in the rhombohedral unit cell and determined its electronic structure and phonon frequencies as a function of temperature. We find that the electronic bands and the phonon frequencies show negligible change as a function of temperature with no anomaly. We also explored if the observed changes in our experiments can be associated with an isostructural phase transition. To find the presence of another local minimum of Sb_2Te_3 within the anomalous temperature range (200–250 K) of Sb_2Te_3, we picked the rhombohedral crystal structure of Sb_2Te_3 at a representative temperature of 215 K from the range of temperature (200–250 K) related to the anomaly and varied the position of one of the two Te layers (which sits at the point of centrosymmetry) within the unit cell, keeping the symmetry of the crystal unchanged. We do find an isostructural metastable state of Sb_2Te_3 which is 0.65 eV/f.u. higher in energy than the ground-state minimum at 215 K. The transition path connecting the stable and metastable structures of Sb_2Te_3 at 215 K determined with the nudged elastic band climbing image (NEB-CI) method reveals that the barrier height for the transition path is too high (5.4 eV) for the phase transition to occur. Thus, the possibility of an isostructural phase transition between the two local minima of Sb_2Te_3 as the origin of the observed anomalies is also ruled out.

As the formation of SFs are expected to be energetically inexpensive in layered materials [39], we explored the formation of SFs as a possible mechanism of the anomalies in the physical properties of layered Sb_2Te_3. We introduce SFs in the basal plane of the hexagonal structure (equivalent to the rhombohedral one) of Sb_2Te_3 and constructed the pristine (with cell vectors $|\vec{\mathbf{a}}_0| = |\vec{\mathbf{b}}_0|$ and $\vec{\mathbf{c}}_0$) and faulted configuration (with cell vectors: $\vec{\mathbf{a}}_{\rm SF} = \vec{\mathbf{a}}_0, \vec{\mathbf{b}}_{\rm SF} = \vec{\mathbf{b}}_0, \vec{\mathbf{c}}_{\rm SF} = \vec{\mathbf{c}}_0 + \frac{1}{3}\vec{\mathbf{a}}_0 + \frac{2}{3}\vec{\mathbf{b}}_0$) of Sb_2Te_3, where $\vec{\mathbf{a}}, \vec{\mathbf{b}}$, and $\vec{\mathbf{c}}$ denote the lattice vectors of the hexagonal unit cell of Sb_2Te_3 [Fig. 3(a)]. We calculated the free energy $F = E_{\rm tot} + F_{\rm vib}$ of these structures as a function of temperature within the harmonic approximation, where $E_{\rm tot}$ is the total energy at 0 K and $F_{\rm vib}$ is the vibrational contribution to the free energy given by $F_{\rm vib} = \frac{k_B T}{N_q}\sum_{iq} \log[2\sinh(\frac{\hbar\omega_{iq}}{2k_B T})]$. Here N_q is the total number of wave vectors q in the Brillouin zone, ω_{iq} is the frequency of the ith phonon with wave vector q obtained using DFT linear response calculations. The

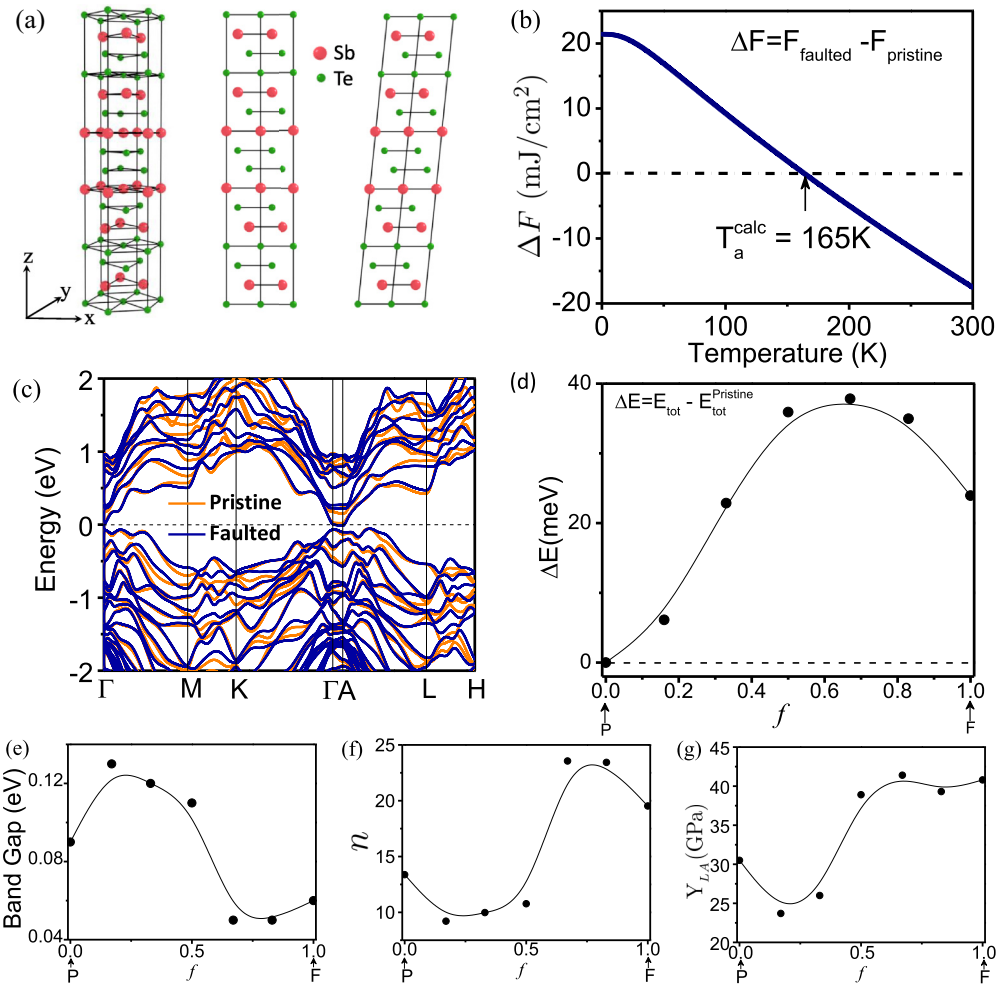

FIG. 3. (a) Hexagonal crystal structure of pristine Sb_2Te_3, its side view and stacking faulted configuration as seen from a side view. (b) Free energy difference (ΔF) of faulted and pristine structures as a function of temperature. (c) Electronic structures of the pristine and faulted configurations of Sb_2Te_3, calculated with spin orbit coupling (SOC). (d) Total energy (setting zero as the energy of the pristine structure) (e) band gap (determined with SOC), (f) calculated refractive index, and (g) longitudinal modulus of elasticity (calculated using $Y_{LA} = \frac{1}{V}\frac{\partial^2 E_{\rm tot}}{\partial \epsilon_{zz}^2}|_{\epsilon_{zz}=0}$, where V is volume of the unit cell, $E_{\rm tot}$ is the total energy obtained with SOC, and ϵ_{zz} is the uniaxial strain) is plotted for the pristine, faulted, and their intermediate configurations along the path parameterized by f. P and F represent the positions of pristine and faulted configurations, respectively.

free energy difference (ΔF) of pristine and faulted structures with optimized cell parameters decreases with temperature and becomes negative at 165 K [Fig. 3(b)]. This means that a structure with infinitely extensive SF stabilizes above $T_a^{\rm calc} = 165$ K. Thus, our first-principles theoretical analysis points out that the observed anomaly in experiments is very likely associated with the formation of SFs in the layered Sb_2Te_3 above T_a. Considering all the approximations, we do not expect the $T_a^{\rm calc}$ [Fig. 3(b)] to match quantitatively the experimental anomaly temperature (~225 K).

To corroborate the mechanism of SFs, we estimated other properties of Sb_2Te_3, at intermediate deformed states along the path connecting the pristine (P) structure to the faulted (F) one, parameterized with f to induce variation in $\vec{\mathbf{c}}$ of the hexagonal cell $\vec{\mathbf{c}} = \vec{\mathbf{c}}_0 + \frac{1}{3} f \vec{\mathbf{a}}_0 + \frac{2}{3} f \vec{\mathbf{b}}_0$ and $0 \leqslant f \leqslant 1$ ($\vec{\mathbf{c}}_0$, $\vec{\mathbf{a}}_0$, and $\vec{\mathbf{b}}_0$ are the pristine hexagonal unit cell lattice parameters). $f = 0$ and $f = 1$ correspond to the pristine and faulted structures, respectively. Figure 3(d) shows the total energy at intermediate configurations along the path of formation of the stacking fault relative to the pristine configuration. The energy difference between the pristine and stacking faulted structure is 24 meV (i.e., 8 meV/f.u.) which is very small compared to the energy of the isostructural transition (i.e., 0.65 eV/f.u.) indicating the formation of the stacking fault to be a possible mechanism. We find that the band gap, refractive index, longitudinal elastic modulus [Figs. 3(e) to 3(g)] vary significantly along the path (as a function of f). The refractive index (n), obtained as $\sqrt{\epsilon_\infty}$ exhibits a dip followed by a sharp rise along the path, qualitatively in agreement with experimental observation near $T_a = 225$ K [Figs. 2(e) and 3(f)]. This rise in the refractive index (n) correlates with a minimum in band gap along the path at $f = 0.67$ [Figs. 3(e) and 3(f)]. We note that the refractive index (n) was estimated using scissor correction based on the calculated band gap obtained after including SOC. Thus, the SOC and the subtle changes in the electronic structure and the band gap during the formation of SFs appear to

be responsible for the observed anomalies. The calculated longitudinal elastic modulus along the path exhibits a peak [Fig. 3(g)] as the faulted structure forms, also consistent with the observed behavior [Fig. 2(h)]. This analysis assumes that SFs start forming in a narrow range of temperature below T_a. The observed anomalous temperature window of 200 to 250 K is associated with the path of formation of SFs in our model.

We now check whether the faulted structure of Sb_2Te_3 has the same electronic topology as that of its pristine structure by exploring the adiabatic continuity between the pristine and the faulted structures. For this, we calculated the electronic structures of configurations at the smoothly deformed intermediate states between the pristine and faulted structures [Fig. 3(c)]. We find that the band gap of intermediate configurations does not close, and hence we do not expect any electronic topological phase transition to occur [Fig. 3(e)]. This implies that the electronic topology of the faulted structure is nontrivial. Hence, a drop in the calculated band gap close to the faulted configuration is responsible for the observed anomalies in the refractive index and longitudinal modulus of elasticity. The temperature dependence of the optical phonon amplitude (B_{OP}), scattering rate (Γ), and frequency ν_{OP} [Figs. 1(d) to 1(f)] show that the system is more anharmonic in the temperature window of 200 to 250 K. It is reasonable to expect that large anharmonicity and disorder both can arise due to SFs [40]. Either or both can be responsible for the phonon softening and linewidth increase near T_a. We are unable to separate their relative contributions at this stage. Further work is required to address this.

The materials of this class are also known for their thermoelectric properties [41–44]. Thermoelectric efficiency can be enhanced by reducing the thermal conductivity (κ_{ph}). As optical phonons are more anharmonic near $\sim T_a$, stacking faults can be engineered in these materials which may scatter the phonons and not the electrons [45]. This can further enhance the existing thermoelectric efficiency of this class of materials.

IV. CONCLUSION

In conclusion, we probed the temperature dependence of photoexcited carriers, optical phonon, and acoustic phonon dynamics in Sb_2Te_3 using ultrafast pulses with particular emphasis in the temperature range near $T_a = 225$ K, where the anomaly in thermal expansion was reported. We observe anomalous behavior in the relaxation dynamics of photoexcited carriers, optical phonons, and acoustic phonons. The anomaly is clearly reflected in the refractive index, sound velocity, and elastic modulus extracted within a strain pulse propagation model. Our first-principles DFT calculations show that the anomalies in the measured quantities are associated with the formation of SFs in the layered structure of Sb_2Te_3, stabilized by vibrational entropy. Above 200 K the electronic structure changes nonmonotonously across the anomaly with no change in the electronic topology. As other three-dimensional topological insulators like Bi_2Te_3 and Bi_2Se_3 are also layered materials, we expect the stacking fault mechanism to be responsible for their anomalous temperature behavior in the appropriate window [9,10].

ACKNOWLEDGMENTS

A.K.S. thanks Dr. Jayaraman for providing single crystals. A.K.S. thanks DST for financial support. G.P. thanks Council of Scientific and Industrial Research (CSIR) for SRF. K.P. thanks JNCASR for a research fellowship. A.K.S. and U.V.W. thank DST for support through J.C. Bose National Fellowships.

[1] J. E. Moore, Nat. Phys. **11**, 897 (2015).
[2] M. Z. Hasan and C. L. Kane, Rev. Mod. Phys. **82**, 3045 (2010).
[3] D. Hsieh, D. Qian, L. Wray, Y. Xia, Y. S. Hor, R. J. Cava, and M. Z. Hasan, Nature (London) **452**, 970 (2008).
[4] D. Hsieh, Y. Xia, D. Qian, L. Wray, F. Meier, J. H. Dil, J. Osterwalder, L. Patthey, A. V. Fedorov, H. Lin, A. Bansil, D. Grauer, Y. S. Hor, R. J. Cava, and M. Z. Hasan, Phys. Rev. Lett. **103**, 146401 (2009).
[5] Y. L. Chen, J. G. Analytis, J.-H. Chu, Z. Liu, S.-K. Mo, X.-L. Qi, H. Zhang, D. Lu, X. Dai, Z. Fang, S. C. Zhang, I. R. Fisher, Z. Hussain, and Z.-X. Shen, Science **325**, 178 (2009).
[6] Y. Xia, D. Qian, D. Hsieh, L. Wray, A. Pal, H. Lin, A. Bansil, D. Grauer, Y. S. Hor, R. J. Cava, and M. Z. Hasan, Nat. Phys. **5**, 398 (2009).
[7] H. Zhang, C.-X. Liu, X.-L. Qi, X. Dai, Z. Fang, and S.-C. Zhang, Nat. Phys. **5**, 438 (2009).
[8] P. Dutta, D. Bhoi, A. Midya, N. Khan, P. Mandal, S. Shanmukharao Samatham, and V. Ganesan, App. Phys. Lett. **100**, 251912 (2012).
[9] X. Chen, H. D. Zhou, A. Kiswandhi, I. Miotkowski, Y. P. Chen, P. A. Sharma, A. L. Lima Sharma, M. A. Hekmaty, D. Smirnov, and Z. Jiang, App. Phys. Lett. **99**, 261912 (2011).
[10] L. Ping-Yuan, C. Yong-Liang, Z. Da-Jin, C. Peng, Z. Yong, D. Shui-Quan, C. Ya-Jing, and Z. Yong, Acta Phys. Sin. **63**, 117301 (2014).
[11] H. J. Zeiger, J. Vidal, T. K. Cheng, E. P. Ippen, G. Dresselhaus, and M. S. Dresselhaus, Phys. Rev. B **45**, 768 (1992).
[12] S. Wu, P. Geiser, J. Jun, J. Karpinski, and R. Sobolewski, Phys. Rev. B **76**, 085210 (2007).
[13] C. Thomsen, H. T. Grahn, H. J. Maris, and J. Tauc, Phys. Rev. B **34**, 4129 (1986).
[14] S. Kumar, L. Harnagea, S. Wurmehl, B. Buchner, and A. K. Sood, Europhys. Lett. **100**, 57007 (2012).
[15] W. Richter and C. R. Becker, Phys. Status Solidi (b) **84**, 619 (1977).
[16] G. C. Sosso, S. Caravati, and M. Bernasconi, J. Phys.: Condens. Matter **21**, 095410 (2009).

[17] W. Richter, A. Krost, U. Nowak, and E. Anastassakis, Z. Phys. B - Condens. Matter **49**, 191 (1982).
[18] K. Norimatsu, M. Hada, S. Yamamoto, T. Sasagawa, M. Kitajima, Y. Kayanuma, and K. G. Nakamura, J. Appl. Phys. **117**, 143102 (2015).
[19] S. Li, H. Huang, W. Zhu, W. Wang, K. Chen, D.-x. Yao, Y. Wang, T. Lai, Y. Wu, and F. Gan, J. Appl. Phys. **110**, 053523 (2011).
[20] Y. D. Glinka, S. Babakiray, T. A. Johnson, M. B. Holcomb, and D. Lederman, Appl. Phys. Lett. **105**, 171905 (2014).
[21] H. Tamaru, K. Ishida, N. Ogawa, Y. Kubo, and K. Miyano, Phys. Rev. B **78**, 075119 (2008).
[22] S. Dhar and C. Desai, Philos. Mag. Lett. **82**, 581 (2002).
[23] H. Cui, I. Bhat, and R. Venkatasubramanian, J. Electron. Mater. **28**, 1111 (1999).
[24] P. G. Klemens, Phys. Rev. **148**, 845 (1966).
[25] M. Balkanski, R. F. Wallis, and E. Haro, Phys. Rev. B **28**, 1928 (1983).
[26] R. A. Cowley, J. Phys. **26**, 659 (1965).
[27] T. E. Stevens, J. Kuhl, and R. Merlin, Phys. Rev. B **65**, 144304 (2002).
[28] Y. Wang, X. Xu, and R. Venkatasubramanian, App. Phys. Lett. **93**, 113114 (2008).
[29] Y. Kim, X. Chen, Z. Wang, J. Shi, I. Miotkowski, Y. P. Chen, P. A. Sharma, A. L. Lima Sharma, M. A. Hekmaty, Z. Jiang, and D. Smirnov, App. Phys. Lett. **100**, 071907 (2012).
[30] E. S. Zouboulis and M. Grimsditch, Phys. Rev. B **43**, 12490 (1991).
[31] W. J. Borer, S. S. Mitra, and K. V. Namjoshi, Solid State Comm. **9**, 1377 (1971).
[32] C. Postmus, J. R. Ferraro, and S. S. Mitra, Phys. Rev. **174**, 983 (1968).
[33] J. S. Dyck, W. Chen, C. Uher, Č. Drašar, and P. Lošt'ák, Phys. Rev. B **66**, 125206 (2002).
[34] O. J. Kim, K. H. Lee, S. W. Han, G. H. Ha, D. H. Kim, and W. H. Yoon, in *24th International Conference on Thermoelectrics*, (IEEE, New York, 2005), p. 331.
[35] QUANTUM-ESPRESSO is a community project for high-quality quantum-simulation software based on density-functional theory and coordinated by P. Giannozzi. See http://www.quantum-espresso.org and http://www.pwscf.org.
[36] J. P. Perdew, K. Burke, and M. Ernzerhof, Phys. Rev Lett. **77**, 3865 (1996).
[37] A. Bera, K. Pal, D. V. S. Muthu, S. Sen, P. Guptasarma, U. V. Waghmare, and A. K. Sood, Phys. Rev. Lett. **110**, 107401 (2013).
[38] K. Pal and U. V. Waghmare, Appl. Phys. Lett. **105**, 062105 (2014).
[39] H. Dittrich and M. Wohlfahrt-Mehrens, Int. J. Inorg. Mater. **3**, 1137 (2001).
[40] Y. Tian, S. Jia, R. J. Cava, R. Zhong, J. Schneeloch, G. Gu, and K. S. Burch, Phys. Rev. B **95**, 094104 (2017).
[41] N. F. Hinsche, B. Yu. Yavorsky, M. Gradhand, M. Czerner, M. Winkler, J. König, H. Böttner, I. Mertig, and P. Zahn, Phys. Rev. B **86**, 085323 (2012).
[42] D. Wright, Nature (London) **181**, 834 (1958).
[43] T. Caillat, M. Carle, P. Pierrat, H. Scherrer, and S. Scherrer, J. Phys. Chem. Solids **53**, 1121 (1992).
[44] B. Poudel, Q. Hao, Y. Ma, Y. Lan, A. Minnich, B. Yu, X. Yan, D. Wang, A. Muto, D. Vashaee, X. Chen, J. Liu, M. S. Dresselhaus, G. Chen, and Z. Ren, Science **320**, 634 (2008).
[45] Y. Tian, G. B. Osterhoudt, S. Jia, R. Cava, and K. S. Burch, Appl. Phys. Lett. **108**, 041911 (2016).